Granular Matter manuscript No.
(will be inserted by the editor)

Granular Leidenfrost effect in microgravity

Harol Torres Menéndez · Achim Sack · Thorsten Pöschel

Received: January 17, 2020/ Accepted: date

Abstract When a container filled by granular material is subjected to vertical vibration in the presence of gravity, under certain conditions a non-monotonous density profile can be observed. This effect which is characteristic for dissipative granular gases, was termed "floating cluster regime" or "granular Leidenfrost effect". Here, we study the behavior of vibro-agitated granular matter in the absence of gravity and identify a corresponding stationary state of the granulate, that is, we provide experimental evidence of the granular Leidenfrost effect under conditions of weightlessness.

Keywords granular matter · floating cluster · Leidenfrost effect · X-ray radiography · microgravity · weightlessness · parabolic flight

1 Introduction

When sprinkling a drop of water onto a hot surface, different behavior can be observed, depending on temperature. For $T \gtrsim 100^o$C, the drop will evaporate rapidly. For $T \gtrsim 220^o$C, however, counterintuitively the drop persists much longer on the hot surface due to a vapor layer formed between the drop and the hot surface, which reduced heat transfer drastically. This phenomenon was first described by Leidenfrost [1,2,3,4,5] and is known as *Leidenfrost effect*.

Although mostly studied with water drops, the Leidenfrost effect can also be observed with stiff sublimable solids, e.g., dry ice [6,7,8,9]. Recently, it was found that hydrogel balls, that is, vaporizable soft solids, float above a hot surface similar to a drop of water when gently deposited [10] but bounce persistently when dropped onto the hot surface [11].

Granular materials, can also exhibit a dynamics similar to the Leidenfrost effect when heated from below in the presence of gravity. Here, the term *heated* refers to the *granular temperature* [12], that is, the supply of energy from below through mechanical vibration. In a certain range of parameters one observes a density inversion which resembles the Leidenfrost effect [13,14,15,16,17], that is, a dilute region of fast particles (analogous to the vapor layer) supports a denser layer of particles (analogous to the water drop). Because of its phenomenologically similarity to the common Leidenfrost effect, Eshuis *et. al.* called this phenomenon *granular Leidenfrost effect* [15].

Obviously, gravity is essential to this effect, however, numerical simulations predict a similar effect when granular matter is confined in a vibrating container in the absence of gravity [18,19,20]. Given a certain filling fraction, independent of the frequency of excitation, for small amplitude, the granular material assumes a gaseous state filling the available volume nearly homogeneously. For large amplitude, a dense layer forms in the center of the box and the space between this layer and the container walls is occupied by a granular gas, see Fig. 1. For yet larger amplitude, the system transits to the *collect and collide regime* [18] where the particles perform a collective motion in harmony with the agitation [21,22,18,23,24,25,26].

Here we present experimental evidence of the existence of the granular Leidenfrost effect in weightlessness. To this end, we study granular dynamics in a cubic box, subjected to sinusoidal oscillations, by means of X-ray radiography. Data have been recorded using the HORUS X-ray facility [27] aboard an airplane performing parabolic flights, in order to achieve weightlessness.

Harol Torres Menéndez · Achim Sack · Thorsten Pöschel
Institute for Multiscale Simulation
Universität Erlangen-Nürnberg, Cauerstraße 3
91058 Erlangen
Germany

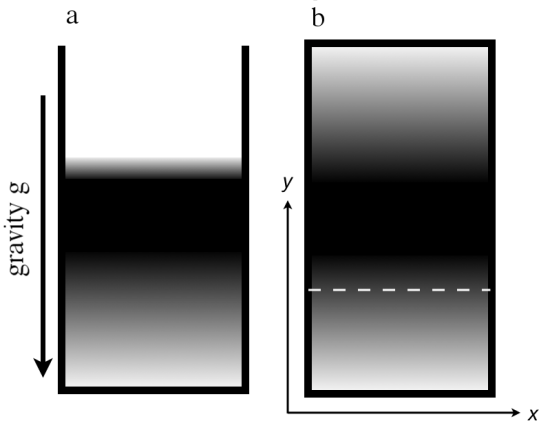

Fig. 1 Sketch of the granular Leidenfrost phenomenon under conditions of gravity (a) and weightlessness (b). In both cases the system is supplied with energy by vibrating the container. Under gravity, the material is heated from below. In weightlessness, vibration of the container implies heating from both sides. We also introduce the coordinate system used in Sec. 3. The dashed line shows the direction of averaging to obtain the profiles of packing fraction and average difference intensity shown in Figs. 4 and 5

2 Experimental setup

The experimental setup is sketched in Fig. 2. A container

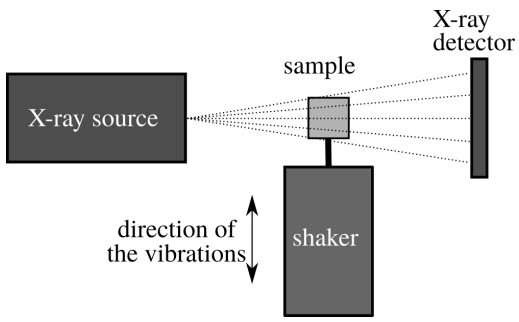

Fig. 2 Sketch of the experimental setup. A container partially filled by granular material was vibrated by an electromagnetic shaker. The behavior of the granulate was recorded by high-speed radiography using the HORUS facility [27]. The experiment was done aboard an airplane performing parabolic flights, in order to achieve weightlessness conditions.

of polymethyl methacrylate (PMMA) of size $5 \times 5 \times 5\,\mathrm{cm}^3$ is partially filled (filling fraction 0.35) with polystyrene (PS) beads of diameter $d = 1\,\mathrm{mm}$ and material density, $\rho = 1.06\,\mathrm{g/cm}^3$. The sample box is agitated by an electromagnetic shaker TIRAvib S 51140 [28], which provides a rated force of up to 400 N. The apparatus is constructed in form of a module for use in the high speed radiography and tomography facility HORUS [27] which can be operated aboard of an airplane performing parabolic flights. Here we used HORUS with the configuration characterized in Tab. 1

Table 1 HORUS configuration

X-ray tube	voltage	110 kV
	current	0.13 mA
detector	exposure time	40 ms
	frame rate	$25\,\mathrm{s}^{-1}$
	pixels resolution	$1944 \times 1536\,\mathrm{px}^2$
	spatial resolution	$75\,\mu\mathrm{m/px}$
	sensitive area	$14.54 \times 11.49\mathrm{cm}^2$
	recorded frames / experiment	1000

To obtain packing density profiles from the radiography images, the X-ray apparatus has to be calibrated. The calibration procedure is non-standard and described in detail in the Appendix.

Performing parabolic flights, each experiment starts in the pull up phase where we encounter conditions of hypergravity, ∼2g. In this phase, the shaker starts to perform sinusoidal vibrations of frequency f and amplitude A. A few seconds before entering the microgravity phase, the X-ray tube is turned on, and the radiographic recording of the experiment starts. The driving parameters of the shaker as well as the X-ray parameters are controlled by an external computer.

3 Results

We studied the granular dynamics for sinusoidal vibration of frequency and peak-to-peak amplitude in the range $f = (5\ldots35)\,\mathrm{Hz}$ and $A = (1\ldots19)\,\mathrm{mm}$, respectively. For $A \gtrsim 5\,\mathrm{mm}$ and independent of the frequency, we found the system in the collect-and-collide regime, where the particles follow collectively the motion of the container due to the external excitation. For $f \lesssim 25\,\mathrm{Hz}$ and $A \lesssim 5\,\mathrm{mm}$ no systematic dynamics could be found, that is, the dynamics was essentially governed by the spurious accelerations due to the imperfections of the microgravity in the airplane. Consequently, these ranges of parameters lead to dynamical patterns which are not subject of the current paper.

For parameters $f \gtrsim 25\,\mathrm{Hz}$ and $A \lesssim 5\,\mathrm{mm}$ we found granular Leidenfrost patterns, that is, a central dense region supported by two gas regions close to the walls, as predicted by numerical simulations [19], provided the residual acceleration was nearly zero which was not the case for all parabulae. Figure 3 shows a sequence of radiographic images for $f = 25\,\mathrm{Hz}$ and $A = 2\,\mathrm{mm}$. Note that only the central region of the sample box of size $0.8 \times 5\,\mathrm{cm}^2$ is shown. We see clearly that the regions close to the upper and lower walls (darkest regions) appear brighter, which, corresponds to low packing density.

Given the limitations of relevant vibration parameters discussed above, during the parabolic flight campaign we studied 5 sets of parameters which correspond to granular Leidenfrost patterns, specified in Table 2. Figure 4 shows the

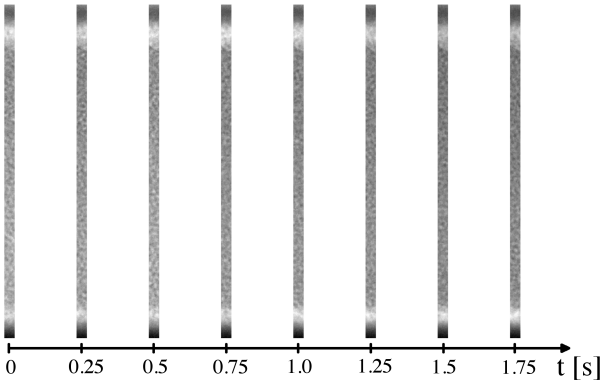

Fig. 3 Sequence of radiographic images of the central region of the sample box of size $0.8 \times 5\,\mathrm{cm}^2$ for sinusoidal vibration at $f = 25\mathrm{Hz}$ and $A = 2\mathrm{mm}$ (peak to peak). The granulate in the sample box consists of 1 mm diameter polystyrene beads of material density $1.06\,\mathrm{g/cm}^3$

Table 2 Studied sets of vibration parameters corresponding to granular Leidenfrost patterns

set of parameters	*I*	*II*	*III*	*IV*	*V*
frequency, f	25 Hz	25 Hz	25 Hz	30 Hz	35 Hz
amplitude, A	2 mm	3 mm	4 mm	2 mm	2 mm

profiles of average packing fraction, φ, for these five sets of shaking parameters. The profiles have been corrected with respect to the effect of spurious residual acceleration in the direction of the vibrations. Such small deviations from the perfectly weightlessness state are caused by imperfections of the parabulae performed by the airplane mainly due to turbulences of the weather conditions.

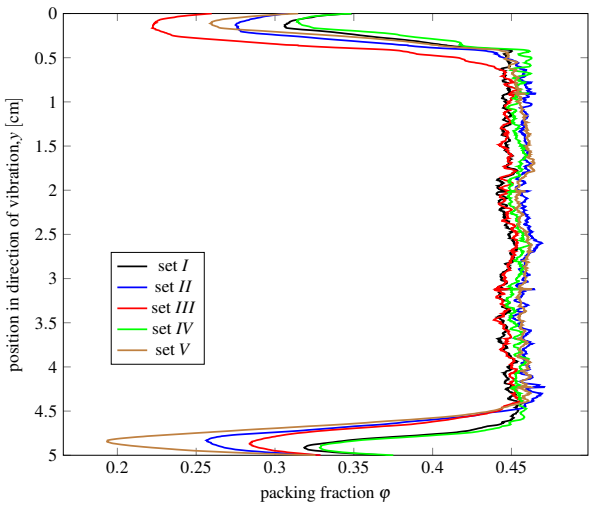

Fig. 4 Profiles of packing fraction, φ, for the sets of vibration parameters specified in Tab. 2. For all sets, the packing fraction in the center part of the container is significantly larger than next to the container walls, signaling the presence of the granular Leidenfrost effect. Positions $y = 0$ and $y = 5\mathrm{cm}$ correspond to the positions of the container walls. The coordinate, y, is drawn on the vertical axis for comparison to the snapshots shown in Fig. 3

For all sets of parameters, we find a region of higher packing fraction, $\varphi \approx 0.45$, in the center part of the container. Close to the walls, the packing fraction was found significantly smaller, the concrete value depends on the parameters of vibration and ranges in the interval $0.2 \lesssim \varphi \lesssim 0.33$ for the sets of parameters studied here. The averaged profiles shown in Fig. 4 are in agreement with the radiographic snapshots shown in Fig. 3 taken for parameters from set *I*. The observed profile of packing fraction evidences the presence of the granular Leidenfrost effect, also in the absence of gravity. For details of the measurement see the Appendix.

For the case of the granular Leidenfrost effect, a dense layer of granular material floats in the center of the container, separated from the walls by cushions of granular gas. Since the granular temperature in a granular solid is much smaller than in a granular gas, the presence of the granular Leidenfrost effect should also leave a fingerprint in the profile of granular temperature or, correspondingly, in the profile of absolute velocity of the particles.

Our X-ray experiment does not allow for tracking individual particles from which we could subsequently determine the velocity profiles using methods like Particle Image Velocimetry (PIV). A non-quantitative impression of the velocity profile can be obtained from the difference of X-ray images obtained at different time, $t, t+T, t+2T, t+3T$ etc., where T is the oscillation period of the external agitation.

A measure of the velocity is then provided by the average difference intensity in the direction of the vibration, $\Delta I_{\Delta t}(y) \equiv \langle\langle|(I(t+\Delta t,x,y) - I(t,x,y))|\rangle_x\rangle_t$, where $I(t,x,y)$, is the intensity of the X-ray measured at the position (x,y) at time t; see Fig. 1 for the used coordinate system. The symbol $\langle\ldots\rangle_x$ stands for averaging along a line in x-direction, that is, in the direction perpendicular to the direction of the vibration and the X-ray beam (see dashed line in Fig. 1). The symbol $\langle\ldots\rangle_t$ stands for averaging over all the data corresponding to the same delay time, Δt.

For data set *I* (see Table 2), Figure 5 shows the profile $\Delta I_{\Delta t}(y)$ for $\Delta t = T$, $\Delta t = 2T, \ldots$, $\Delta t = 5T$. Close to the center of the container we find small values of the intensity difference, indicating only slow changes of the images due to small velocity of the particles. In the vicinity of the walls, values of the profile $\Delta I_{\Delta t}(y)$ increase steeply, indicating large velocity of the particles next to the walls. While close to the center the curves collapse for $\Delta t > 2T$, due to small granular temperature in the floating layer of granulate, close to the walls the values of the profile grow approximately proportionally to Δt due to steady motion of the particles in the gas state. Profiles similar to Fig. 5 were obtained also for the other sets of parameters listed in Tab. 2.

While the data shown in Fig. 5 do not allow for a quantitative measurement of the granular temperature or the absolute particle velocities, the profiles agree qualitatively with the profile of packing fraction shown in Fig. 4, thus, provid-

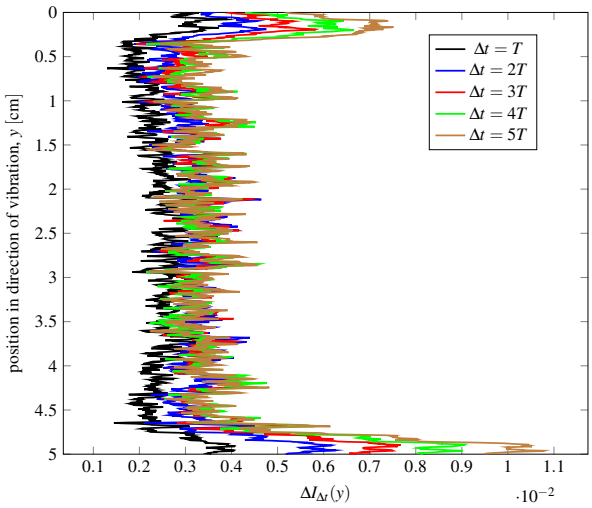

Fig. 5 Profile of the averaged difference intensity, $\Delta I_{\Delta t}(y)$ for different delay time, Δt, obtained from the X-ray images due to parameter set I, see Table 2. The positions $y = 0$ and $y = 5$cm correspond to the positions of the container walls. The coordinate, y, is drawn on the vertical axis for comparison to the snapshots shown in Fig. 3

ing further support of the observation of the granular Leidenfrost effect in weightlessness.

4 Conclusions

We provide experimental evidence for the occurrence of the granular Leidenfrost effect under weightlessness conditions. To this end, we recorded X-ray radiograms of a container partially filled with polystyrene beads and agitated through sinusoidal oscillations during parabolic flights. For the X-ray recording we used the high speed radiography and tomography facility HORUS [27].

For amplitude $A \lesssim 5$ mm peak-to-peak and frequency $f \gtrsim 25$ Hz, a layer of particles of packing fraction $\varphi \approx 0.45$ was formed in the center of the box, while the regions closer to the walls (with respect to the direction of the vibrations) are populated by a granular gas of much lower packing fraction. At the same time we notice that the average absolute particle velocity is much larger next to the walls as compared to the values at the center of the box.

The phenomenon was found to be extremely sensitive to spurious residual accelerations of the plane, nevertheless, both profiles, density and velocity, as well as the sequence of X-ray images, shown in Figs. 3, 4, 5 support each other and provide evidence for the occurrence of the granular Leidenfrost phenomenon under microgravity conditions.

Acknowledgements We thank Dr. Matthias Schröter for fruitful discussions and the German Aerospace Center, DLR, for financial support through the grant HORUS 50WM1643. We thank the support of Novespace during the 30th DLR parabolic flight campaign in Bordeaux where the presented data were recorded.

Conflict of interest

The authors declare that they have no conflict of interest.

References

1. J. G. Leidenfrost. *De Aquae Communis Nonullis Qualitatibus Tractatus*. Ovenius, Duisburg on Rhine, 1756.
2. B. S. Gottfried, C. J. Lee, and K. J. Bell. The Leidenfrost phenomenon: film boiling of liquid droplets on a flat plate. *International Journal of Heat and Mass Transfer*, 9(11):1167 – 1188, 1966.
3. G. S. Emmerson. The effect of pressure and surface material on the Leidenfrost point of discrete drops of water. *International Journal of Heat and Mass Transfer*, 18(3):381 – 386, 1975.
4. A. L. Biance, C. Clanet, and D. Quéré. Leidenfrost drops. *Physics of Fluids*, 15(6):1632–1637, 2003.
5. S. Hidalgo-Caballero, Y. Escobar-Ortega, and F. Pacheco-Vázquez. Leidenfrost phenomenon on conical surfaces. *Physical Review Fluids*, 1(5):051902, Sep 2016.
6. G. Lagubeau, M. Le Merrer, C. Clanet, and D. Quéré. Leidenfrost on a ratchet. *Nature Physics*, 7(5):395–398, 2011.
7. J. C. Burton, P. Y. Lu, and S. R. Nagel. Collision dynamics of particle clusters in a two-dimensional granular gas. *Physical Review E*, 88:062204, Dec 2013.
8. G. G. Wells, R. Ledesma-Aguilar, G. McHale, and K. Sefiane. A sublimation heat engine. *Nature Communications*, 6(1):6390, 2015.
9. S. Dorbolo, N. Vandewalle, and B. Darbois Texier. Spontaneous rotation of an ice disk while melting on a solid plate. *Physics of Fluids*, 28(12):123601, 2016.
10. S. R. Waitukaitis, K. Harth, and M. van Hecke. From bouncing to floating: The Leidenfrost effect with hydrogel spheres. *Physical Review Letters*, 121:048001, Jul 2018.
11. S. R. Waitukaitis, A. Zuiderwijk, A. Souslov, C. Coulais, and M. van Hecke. Coupling the Leidenfrost effect and elastic deformations to power sustained bouncing. *Nature Physics*, 13(11):1095–1099, 2017.
12. N. V. Brilliantov and T. Pöschel. *Kinetic Theory of Granular Gases*. Oxford University Press, Oxford, 2004.
13. Y. Lan and A. D. Rosato. Macroscopic behavior of vibrating beds of smooth inelastic spheres. *Physics of Fluids*, 7:1818–1831, 1995.
14. B. Meerson, T. Pöschel, and Y. Bromberg. Close-packed floating clusters: Granular hydrodynamics beyond the freezing point? *Physical Review Letters*, 91:024301, 2003.
15. P. Eshuis, K. van der Weele, D. van der Meer, and D. Lohse. Granular Leidenfrost effect: Experiment and theory of floating particle clusters. *Physical Review Letters*, 95:258001, 2005.
16. P. Eshuis, K. van der Weele, D. van der Meer, R. Bos, and D. Lohse. Phase diagram of vertically shaken granular matter. *Physics of Fluids*, 19:123301, 2007.
17. E. W. C. Lim. Density segregation in vibrated granular beds with bumpy surfaces. *AIChE Journal*, 56:2588–2597, 2010.
18. M. N. Bannerman, J. E. Kollmer, A. Sack, M. Heckel, P. Müller, and T. Pöschel. Movers and shakers: Granular damping in microgravity. *Physical Review E*, 84:011301, 2011.
19. E. Opsomer, F. Ludewig, and N. Vandewalle. Dynamical regimes of a granular gas in microgravity : a molecular dynamics study. *Journal of Physics*, 327, 2011.
20. E. Opsomer, F. Ludewig, and N. Vandewalle. Dynamical clustering in driven granular gas. *Europhysics Letters*, 99:40001, 2012.
21. M. Hou, R. Liu, G. Zhai, Z. Sun, and K. Lu. Velocity distribution of vibration-driven granular gas in Knudsen regime in microgravity. *Microgravity Science and Technology*, 20:73–80, 2008.

22. K. Harth, U. Kornek, T. Trittel, U. Strachauer, S. Höme, K. Will, and R. Stannarius. Granular gases of rod-shaped grains in microgravity. *Physical Review Letters*, 110:144102, 2013.
23. A. Sack, M. Heckel, J. E. Kollmer, F. Zimber, and T. Pöschel. Energy dissipation in driven granular matter in the absence of gravity. *Physical Review Letters*, 111:018001, 2013.
24. A. Sack, M. Heckel, J. E. Kollmer, and T. Pöschel. Probing the validity of an effective-one-particle description of granular dampers in microgravity. *Granular Matter*, 17:73–82, 2014.
25. J. E. Kollmer, M. Tupy, M. Heckel, A. Sack, and T. Pöschel. Absence of subharmonic response in vibrated granular systems under microgravity conditions. *Physical Review Applied*, 3:024007, 2015.
26. A. Sack, C. R. K. Windows-Yule, M. Heckel, D. Werner, and T. Pöschel. Granular dampers in microgravity - Sharp transition between modes of operation. *preprint*, 2020.
27. H. Torres Menéndez, M. Heckel, A. Sack, and T. Pöschel. X-ray tomography in micro-gravity. *Review of Scientific Instruments*, 90(10):105103, 2019.
28. Tira. Vibration test systems (shakers) 9N to 400N.
29. P. Bouguer. *Essai d'optique sur la gradation de la lumière*. Claude Jombert, Paris, 1729.
30. J. H. Lambert. *Photometria sive de mensura et gradibus luminis, colorum et umbrae*. Augsburg. Klett, 1760.
31. A. Beer. Bestimmung der Absorption des rothen Lichts in farbigen Flüssigkeiten. *Annalen der Physik*, 162:78–88, 1852.
32. J. D. Ingle Jr. and S. R. Crouch. *Spectrochemical analysis*. Prentice-Hall, United States, 1988.
33. J. Als-Nielsen and D. McMorrow. *Elements of Modern X-ray Physics, 2nd Edition*. Wiley, 2011.
34. J. H. Hubbell and S. M. Seltzer. X-ray mass attenuation coefficients. https://physics.nist.gov/PhysRefData/XrayMassCoef/tab2.html, 2004.
35. M. Baur, N. Uhlmann, T. Pöschel, and M. Schröter. Correction of beam hardening in *x*-ray radiograms. *Review of Scientific Instruments*, 90:025108, 2019.
36. M. Baur, J. Claussen, S. Gerth, J. E. Kollmer, T. Shreve, N. Uhlmann, and T Pöschel. How to measure the volume fraction of granular assemblies using x-ray radiography. *Powder Technology*, 356:439 – 442, 2019.

Appendix: Calibration of X-ray radiography

On their way from the source to the detector, X-rays are attenuated due to the presence of matter, that is, the particles and the container material. For monochromatic X-rays, the intensity $I(\xi)$ after passing through a homogeneous material layer of thickness ξ obeys the Lambert-Beer equation [29, 30, 31, 32, 33]

$$I(\xi) = I_0 e^{-\mu(E,Z)\xi} \tag{1}$$

where I_0 is the intensity of the incident beam and μ is the attenuation coefficient which depends on the frequency (energy), E, of the beam and on the radiographed material, in particular characterised by the atomic number, Z. Knowing the parameter μ for the particle material and the container walls, Eq. (1) can be used to determine for each pixel on the detector the total amount of material, ξ, the beam penetrates. For the case of a solid material, such as the container walls, ξ would be simply the actual thickness of the radiographed object. In case of a granular material, however, ξ is the total length of particle material the beam penetrates, that is, the length of the path through the granular material reduced by the voids, provided we can neglect the attenuation of the X-rays by the material filling the voids which is typically air. Thus, for a granular material or other porous objects, from ξ we can determine the average volume fraction via $\varphi = \xi/L$ where L is the total length passed by the beam, e.g. the space between the side walls of the container, accommodating the granulate.

On the way from the source to the detector, the X-rays cross two times the container wall of width d and the particles of the granulate, summing up to the total width ξ. Thus

$$I(\xi) = I_0 e^{-\mu_{\mathrm{PMMA}}(E,Z_{\mathrm{PMMA}})2d} e^{-\mu_{\mathrm{PS}}(E,Z_{\mathrm{PS}})\xi} = \hat{I}_0 e^{-\mu_{\mathrm{PS}}(E,Z_{\mathrm{PS}})\xi}\,, \tag{2}$$

where μ_{PMMA} and μ_{PS} are the attenuation coefficients of the container and particle materials and the constant $\hat{I}_0$ is defined by Eq. (2). Physically, the material of the object determines the value of μ via the character of the scattering atoms, described by their atomic number, Z, and the density of atoms met per unit distance traveled by the beam. The latter quantity is determined by the material density. While for standard conditions (temperature, pressure, etc.) the density is a constant material property, in some cases it is necessary to take the concrete value of density into account, for instance when thermal expansion due to changing temperature is considered. Obviously, the number of scatterers per unit length is proportional to density, therefore, we better write $\mu(E,Z,\rho)$ highlighting the dependence on density. Introducing the *mass attenuation coefficient*, $\overline{\mu}$,

$$\mu(E,Z,\rho) = \overline{\mu}(E,Z)\rho\,, \tag{3}$$

Eq. (2) reads

$$I(\xi) = \hat{I}_0 e^{-\overline{\mu}_{\mathrm{PS}}(E,Z_{\mathrm{PS}})\rho_{\mathrm{PS}}\xi}\,. \tag{4}$$

Equation (4) can be used for situations where ρ is not constant, but also in a different way which we will exploit below. Assume two materials A and B are similar enough with respect to their Z but different in density, thus,

$$\overline{\mu}_{\mathrm{A}} \approx \overline{\mu}_{\mathrm{B}}, \qquad \text{that is} \quad \mu_{\mathrm{B}} = \mu_{\mathrm{A}}\frac{\rho_{\mathrm{B}}}{\rho_{\mathrm{A}}}\,. \tag{5}$$

For most materials, except pure and mono-isotopic elements, there is no unique atomic number Z but the material is a well defined stoichiometric mixture of atoms. Therefore, instead of Z one should consider an effective number $\langle Z/A\rangle$ where A takes the composition of the material into account. For the case of poly-isotopic elements, the averaging, $\langle\ldots\rangle$, extends over all isotopes weighted by their respective abundance on

Earth. For other materials also the chemical composition has to be taken into account for averaging. For details see [34].

Consider now the two materials of interest for the current experiment, the wall material, PMMA, and the particle material, PS. We find [34]

$$\begin{aligned}\langle Z/A\rangle_{\mathrm{PMMA}} &\approx 0.539\\ \langle Z/A\rangle_{\mathrm{PS}} &\approx 0.537\,,\end{aligned} \tag{6}$$

that is, the values agree up to the thousandths digit. Therefore, the approximation

$$\mu_{\mathrm{PS}} \approx \mu_{\mathrm{PMMA}} \frac{\rho_{\mathrm{PS}}}{\rho_{\mathrm{PMMA}}} \tag{7}$$

with $\rho_{\mathrm{PS}} \approx 1.19\,\mathrm{g/cm^3}$ and $\rho_{\mathrm{PMMA}} \approx 1.06\,\mathrm{g/cm^3}$ is well justified and Eq. (4) can be written as

$$-\log\left(\frac{I(\xi)}{\hat{I}_0}\right) = \mu_{\mathrm{PMMA}} \frac{\rho_{\mathrm{PS}}}{\rho_{\mathrm{PMMA}}}\,\xi \tag{8}$$

. We will use this relation below.

Equation (1) and consequently also Eq. (8) hold true for the case of monochromatic light, however, commercial X-ray tubes emit a polychromatic *Bremsstrahlung*-spectrum. Therefore, Eq. (8) cannot be directly applied. Instead, the frequencies of the X-ray are attenuated differently, such that, the spectral composition changes when polychromatic light penetrates matter. In fact, low frequencies are attenuated more than high frequencies such that the spectrum is shifted towards high frequencies. This phenomenon is referred to as *beam hardening*, and the measured thickness, ξ, and, thus, the measured packing fraction in granular matter must be corrected for this effect [35,36].

To this end, $\mu(E,Z)$ in Eq. (1) is replaced by an effective attenuation coefficient, μ^{eff}, which depends not only on the parameters of the radiographed material, but also on its thickness in the direction of the X-rays beam, ξ, and on the specific properties of the X-rays and the detector used, for details see [35,36]. Again, ξ stands for the extension of the granulate reduced by the voids between the grains. Therefore

$$-\log\left(\frac{I(\xi)}{\hat{I}_0}\right) = \mu^{\mathrm{eff}}_{\mathrm{PMMA}}(\xi)\,\frac{\rho_{\mathrm{PS}}}{\rho_{\mathrm{PMMA}}}\,\xi\,, \tag{9}$$

where again ξ is the extension of the granular material (container clearance) reduced by voids between the particles. For the effective attenuation coefficient, Baur *et al.* [35,36] proposed the heuristic formula

$$\mu_{\mathrm{eff}}(\ell) = a + \frac{b}{\ell^{\alpha}}\,, \tag{10}$$

whose parameters a, b, and α have to be calibrated, in order to use Eq. (9) for measuring ξ via $I(\xi)$.

Given that the relevant material properties of the particles material, PS, and the wall material, PMMA, are very similar, we use the arguments above and calibrate the parameters of $\mu^{\mathrm{eff}}_{\mathrm{PMMA}}$ by means of test measurements of the intensity of the X-rays after traveling through PMMA plates of known thickness ℓ, using the X-ray settings specified in Table 1. Figure 6 shows the calibration measurements together with a fit to Eq. (10). The best fit is obtained for the parameters $a = 0.0$, $b = 0.378$, and $\alpha = 0.180$.

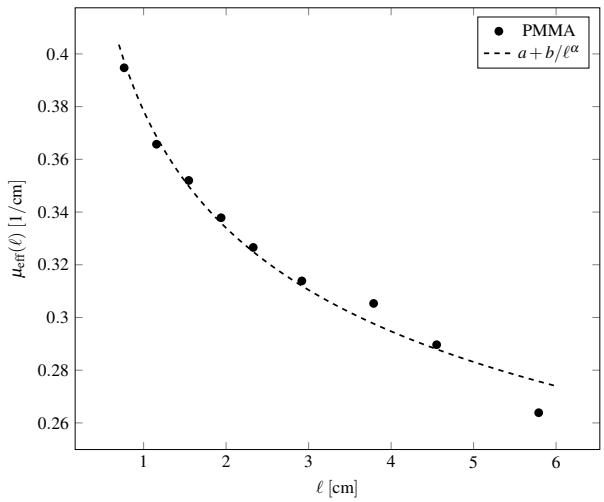

Fig. 6 Effective attenuation coefficient, $\mu^{\mathrm{eff}}_{\mathrm{PMMA}}$ as a function of the material thickness, ℓ, obtained from calibration measurements for material of known thickness. Since PMMA and PS have very similar material properties relevant for X-ray attenuation, the calibration was made with PMMA plates of known width. The best fit of Eq. (10) was obtained for $a = 0.0$, $b = 0.378$, and $\alpha = 0.180$ (dashed line)

Once the function $\mu^{\mathrm{eff}}_{\mathrm{PMMA}}$ is known, Eq. (9) can be solved numerically for the material thickness, ξ. The profile of the packing fraction, $\varphi(y)$ is then obtained via $\varphi(y) = \langle \xi/L\rangle_x$, where L is the inner length of the container in the direction of the X-ray beam (5 cm in our case), and the symbol $\langle\ldots\rangle_x$ stands for averaging along a line perpendicular to both the direction of the vibration and the of X-ray beam, see dashed line in Fig. 1.